Photoacoustics 23 (2021) 100285

Contents lists available at ScienceDirect

Photoacoustics

journal homepage: www.elsevier.com/locate/pacs

In-vitro and *in-vivo* characterization of CRANAD-2 for multi-spectral optoacoustic tomography and fluorescence imaging of amyloid-beta deposits in Alzheimer mice

Ruiqing Ni [a,b,c,*], Alessia Villois [d], Xose Luis Dean-Ben [a,e], Zhenyue Chen [a,e], Markus Vaas [a], Stavros Stavrakis [d], Gloria Shi [a], Andrew deMello [d], Chongzhao Ran [f], Daniel Razansky [a,c,e], Paolo Arosio [d], Jan Klohs [a,c,*]

[a] Institute for Biomedical Engineering, ETH & University of Zurich, Zurich, Switzerland
[b] Institute for Regenerative Medicine, University of Zurich, Zurich, Switzerland
[c] Zurich Neuroscience Center (ZNZ), Zurich, Switzerland
[d] Institute for Chemical and Bioengineering, Department of Chemistry, ETH Zurich, Zurich, Switzerland
[e] Institute of Pharmacology and Toxicology, University of Zurich, Switzerland
[f] Martinos Center for Biomedical Imaging, Massachusetts General Hospital, Harvard Medical School, Charlestown, MA, USA

ARTICLE INFO

Keywords:
Alzheimer's disease
Amyloid-beta
Animal model
Fluorescence imaging
Multi-spectral optoacoustic tomography

ABSTRACT

The abnormal deposition of fibrillar beta-amyloid (Aβ) deposits in the brain is one of the major histopathological hallmarks of Alzheimer's disease (AD). Here, we characterized curcumin-derivative CRANAD-2 for multi-spectral optoacoustic tomography and fluorescence imaging of brain Aβ deposits in the arcAβ mouse model of AD cerebral amyloidosis. CRANAD-2 showed a specific and quantitative detection of Aβ fibrils *in vitro,* even in complex mixtures, and it is capable of distinguishing between monomeric and fibrillar forms of Aβ. *In vivo* epi-fluorescence microscopy and optoacoustic tomography after intravenous CRANAD-2 administration demonstrated higher cortical retention in arcAβ compared to non-transgenic littermate mice. Immunohistochemistry showed co-localization of CRANAD-2 and Aβ deposits in arcAβ mouse brain sections, thus verifying the specificity of the probe. In conclusion, we demonstrate suitability of CRANAD-2 for optical detection of Aβ deposits in animal models of AD pathology, which facilitates mechanistic studies and the monitoring of putative treatments targeting Aβ deposits.

1. Introduction

The abnormal acculumation and the spread of amyloid-beta (Aβ) deposits play a central role in the pathogenesis of Alzheimer's disease (AD) and leads to downstream pathophysiological events [1,2]. Positron emission tomography (PET) imaging of aberrant Aβ deposits has been established as a diagnostic pathological biomarker for AD under clinical setting and been included in the new diagnostic criteria [3]. Three amyloid imaging probes have been approved for clinical usage including ^{18}F-florbetapir [4], ^{18}F-florbetaben [5] and ^{18}F-flumetamol [6]. Higher PET imaging of cortical Aβ loads were reported in the brains from patients with AD and mild cognitive impairment compared to healthy controls [7,8]. While PET imaging in small rodents has been used for studying Aβ-related disease mechanisms and for developing therapeutic strategies [9–15], it has the disadvantages that it requires extensive infrastructure for the generation of dedicated radiotracers and has a low spatial resolution (1 mm) relative to the mouse brain dimension (10 mm × 8 mm).

Optical imaging techniques such as near-infrared fluorescence (NIRF) imaging and multi-spectral optoacoustic tomography (MSOT) imaging have emerged, enabling the *in vivo* imaging of physiological, metabolic and molecular function [16–23]. This is mainly due to the fact that optical techniques are cost-effective, do not require an extensive infrastructure and use stable labels that allow validation of imaging findings with histology. Progress is made not only in the development of optical instrumentation and reconstruction algorithms, but also in the design and synthesis of novel Aβ imaging probes [24]. For example, several probes have been reported for NIRF imaging including NIAD-4

* Corresponding authors at: Institute for Biomedical Engineering, ETH & University of Zurich, Vladimir-Prelog-Weg 4, 8093, Zurich, Switzerland.
E-mail addresses: ruiqing.ni@uzh.ch (R. Ni), klohs@biomed.ee.ethz.ch (J. Klohs).

https://doi.org/10.1016/j.pacs.2021.100285
Received 20 October 2020; Received in revised form 9 June 2021; Accepted 13 July 2021
Available online 15 July 2021

[25], AOI-987 [26], BODIPY [27], THK-265 [28], DANIR [29–32], curcumin-derivatives CRANAD series [33,34], luminescent conjugated oligothiophenes [35,36] and DBA-SLOH [37]. NIRF imaging of Aβ deposits has been shown using a variety of AD mouse models [26,30–34, 37,38]. Despite its advantages, the diffuse nature of light propagation in highly scattering tissue prevents the accurate determination of probe distribution and concentration from NIRF measurements. As an inherent hybrid method, MSOT imaging capitalizes on absorption of light as a source of contrast, while emitted non-radioactive decay broadband ultrasound is used for image formation, thus combining the high sensitivity of optical imaging with the high spatial resolution of ultrasound imaging. Recently, volumetric multispectral optoacoustic tomography (vMSOT) has been introduced with added multiplexing and real-time 3D imaging capabilities, thus enabling a wide range of new biomedical applications [39–44]. Previously, intravital optoacoustic imaging of Aβ deposits with intrathecal injection of Congo Red [27] and croconium-derivative [45] in amyloidosis mouse models have been reported.

In the present study, we show that CRANAD-2, previously used for NIRF imaging [33,34], is suitable for MSOT imaging and describe its utility for *in vivo* whole brain mapping of Aβ deposits in arcAβ mouse model of cerebral amyloidosis [46]. Capitalizing on the fluorescent properties we characterized binding of the probe to Aβ fibrils *in vitro* using a fluorescence binding assays, *in situ* with tissue sections and immunohistochemistry and by cross-validation between MSOT and hybrid fluorescence imaging [47,48]. Our results demonstrate suitability of CRANAD-2 for NIRF and MSOT imaging of Aβ deposits.

2. Materials and methods

2.1. Animal model

Seven transgenic arcAβ mice overexpressing the human APP695 transgene containing the Swedish (K670N/M671L) and Arctic (E693G) mutations under the control of prion protein promoter and five age-matched non-transgenic littermates of both sexes were used (18–24 months-of-age) [46]. ArcAβ mice are characterized by a pronounced amyloid deposition, cerebral amyloid angiopathy and vascular dysfunction [43,49–53]. Animals were housed in ventilated cages inside a temperature-controlled room, under a 12 -h dark/light cycle. Pelleted food (3437PXL15, CARGILL) and water were provided *ad-libitum*. Paper tissue and red Tecniplast mouse house® (Tecniplast, Milan, Italy) shelters were placed in cages as environmental enrichments. All experiments were performed in accordance with the Swiss Federal Act on Animal Protection and were approved by the Cantonal Veterinary Office Zurich (permit number: ZH082/18).

2.2. In vitro binding between amyloid probes and recombinant $A\beta_{1-42}$ fibrils measured by spectrofluorometer

(T-4)-[(1E,6E)-1,7-Bis[4-(dimethylamino)phenyl]-1,6-heptadiene-3,5-dionato-kO$_3$,kO$_5$] difluo-roboron (CRANAD-2) [33] was purchased from Sigma-Aldrich AG, Switzerland. The emission spectrum and excitation spectrum were measured by using F-4500 FL Spectrophotometer using CRANAD-2 25 μM in phosphate buffered saline (PBS, pH 7.4). For the measurement of emission spectrum, the excitation is set at 640 nm, emission wavelengths were recorded between 680−900 nm. For the measurement of excitation spectrum, the emission is set at 820 nm, excitation wavelengths were measured between 500−750 nm. Recombinant $A\beta_{1-42}$ peptides were expressed in *E.coli* as described previously [54]. $A\beta_{1-42}$ fibrils were formed by incubating a solution of freshly purified 2 μM $A\beta_{1-42}$ monomers in phosphate buffer (20 mM sodium phosphate, 0.2 mM ethylenediaminetetraacetic acid, pH 8.0). The aggregation process was monitored by a quantitative fluorescence assay based on the Thioflavin T (ThT) dye [55]. CRANAD-2 stock was dissolved in dimethyl sulfoxide (DMSO, Sigma-Aldrich AG). The *in vitro* binding between CRANAD-2 (0.1 μM) or ThT (20 μM) with $A\beta_{1-42}$ fibrils (0−0.2 μM) was measured on a spectrofluorometer (Fluoromax-4, HORIBA Jobin Yvon Technologies, Japan) by recording the emission spectra in the range from 660 nm to 800 nm after excitation at 640 nm, or in the range from 450 nm to 650 nm respectively after the excitation at 440 nm. The lower concentration of CRANAD-2 was selected to avoid precipitation. To investigate whether CRANAD-2 binds selectively $A\beta_{1-42}$ fibrils, we assessed the binding of CRANAD-2 (0.1 μM) and ThT (20 μM) to other targets that are rich in β-sheet structures including bovine serum albumin, monoclonal antibody, and amyloids formed by lysozyme, α-synuclein and insulin, all at 0.2 μM. Moreover, we assessed whether CRANAD-2 can distinguish between different conformations of Aβ by measuring binding also to $A\beta_{1-42}$ monomers. Finally, the specificity of CRANAD-2 for $A\beta_{1-42}$ fibrils was further evaluated by measuring the binding between the probe and $A\beta_{1-42}$ fibrils (0−0.2 μM) spiked in a cell lysate obtained from *E.coli* with a total protein concentration of 7 μM.

2.3. MSOT

Cross-sectional MSOT imaging was performed with a commercial inVision 128 small animal scanner (iThera Medical, Germany) as described [56]. Briefly, a tunable (680−980 nm) optical parametric oscillator pumped by an Nd:YAG laser provides 9 ns excitation pulses at a framerate of 10 Hz with a wavelength tuning speed of 10 ms and a peak pulse energy of 100 mJ at 730 nm. Ten arms, each containing an optical fiber bundle, provide even illumination of a ring-shaped light strip with a width of approx. 8 mm. For ultrasound detection, 128 cylindrically focused ultrasound transducers with a center frequency of 5 MHz (60 % bandwidth), organized in a concave array of 270° angular coverage and a curvature radius of 4 cm, were used. Phantom and *in vivo* MSOT images were acquired at 10 wavelengths, *i.e.* 680, 685, 690, 695, 700, 715, 730, 760, 800 and 850 nm, coronal section, averages = 10, field-of-view = 20 mm × 20 mm, resolution = 100 μm × 100 μm, a step size = 0.3 mm moving along the axial direction.

For *in vivo* MSOT, five arcAβ mice and four non-transgenic littermates were imaged with MSOT *in vivo*. Mice underwent also magnetic resonance imaging (MRI) for co-registration with MSOT data and to facilitate volume-of-interest (VOI) analysis. Mice were anesthetized with an initial dose of 4 % isoflurane (Abbott, Cham, Switzerland) in oxygen/air (200/800 mL/min) mixture and were maintained at 1.5 % isoflurane in oxygen/air (100/400 mL/min). The fur over the head was depilated. The mouse was placed in a mouse holder in prone position. The holder was inserted in an imaging chamber filled with water to keep body temperature within 36.5 ± 0.5 °C. Mice were injected intravenously with CRANAD-2 (2.0 mg/kg, 15 % DMSO + 70 % PBS pH 7.4 + 15 % Kolliphor EL, Sigma-Aldrich AG) through the tail vein. Datasets were recorded before, 20, 40, 60, 90, and 120 min after the injection.

MSOT images were reconstructed using a model-based algorithm, size 20 mm, resolution 100 μm, and filter range from 50 kHz to 7 MHz. The model-based reconstruction incorporates a detailed model of detection geometry that allows for more quantifiable images.

2.4. Hybrid vMSOT-fluorescence imaging

A hybrid vMSOT-fluorescence imaging system [39,57] was used to assess one arcAβ mouse. The MSOT system acquired 2D planar images (with 0.3 mm gap between each scan), with the acquisition window (20 mm × 20 mm) moving along the rostral to caudal axis of the mouse brain. VMSOT obtained 3D volumetric images with fixed positioning of the mice. A short-pulsed (<10 ns) laser was used to provide an approximately uniform illumination profile on the mouse brain surface with optical fluence < 20 mJ/cm^2. The excited OA responses were collected with a custom-made spherical array (Imasonic SaS, Voray, France) of 512 ultrasound detection elements with 7 MHz central frequency and > 80 % bandwidth. A custom-made optical fiber bundle

(Ceramoptec GmbH, Bonn, Germany) with 4 outputs was used for guiding the laser beam from multiple angles through the lateral apertures of the array. The detected signals were digitized at 40 mega-samples per second with a custom-made data acquisition system (DAQ, Falkenstein Mikrosysteme GmbH, Taufkirchen, Germany) triggered with the Q-switch output of the laser. The pulse repetition frequency of the laser was set to 100 Hz and the laser wavelength tuned between 660 and 850 nm (10 nm step) on a per pulse basis. For the concurrent 2D epi-fluorescence imaging [48], beam from the pulsed OPO laser was similarly used for excitation. The generated fluorescence field was collected by a fiberscopic imaging fiber bundle comprised of 100,000 fibers and then projected onto an EMCCD camera (Andor Luca R, Oxford Instruments, UK). The fiberscope was inserted into the central aperture of the spherical array detector. The system has an overall field-of-view of 15 mm × 15 mm × 15 mm and resolution in the 110 μm range for vMSOT and 44 μm for epi-fluorescence measurements [39,58]. The optoacoustic signals were recorded before injection, 20, 40, 60, 90 and 120 min after injection of CRANAD-2; fluorescence signals were recorded before injection, 22, 42, 62, 92 and 120 min after injection of CRANAD-2. To examine the influence of scalp on the absorbance intensity, the scalp of the mouse was then removed. The mouse head was imaged afterwards using the same setting.

To assess the fluorescence and OA signals of CRANAD-2 binding to recombinant $A\beta_{42}$, the vMSOT-fluorescence imaging system was used. The spherical array was positioned pointing upwards and filled with agar gel (1.5 %) to guarantee acoustic coupling, which served as a solid platform to place the tubing. One transparent bore polythene tubing (0.28 mm inner diameter, 0.61 mm outer diameter, Smiths Medical) of 15 cm length were fixed on the solid agar gel circular platform (diameter 5 cm) as described earlier [58]. This is to ensure using same condition during measurement for each sample. Uniform illumination of the tubing was achieved by inserting three arms of the fiber bundle in the lateral apertures of the array and a fourth one providing light delivery from the top. The pulse repetition frequency of the laser was set to 100 Hz and the laser wavelength tuned between 550 and 680 nm (5 nm step) on a per pulse basis. Beam from the pulsed OPO laser was similarly used for excitation. The tubing was sequentially filled (using syringe) with CRANAD-2 (1, 3 μM) without and with the presence of Aβ (1, 2 μM). We chose 1–2 μM concentration of Aβ to mimic the accumulation in brain of arcAβ mouse brain based on results from previous MSD and biochemical assays [46,51]. Tubing was flushed with dd water twice between samples. The measurement was repeated three times. All recorded OA signals were normalized with the calibrated wavelength-dependent energy of the laser pulse.

Images were rendered in real-time during the acquisition *via* fast back-projection-based image reconstruction implemented on a graphics processing unit [59]. A 3D model-based iterative algorithm was used off-line for more accurate reconstruction [60]. Prior to reconstruction, the collected signals were band-pass filtered with cut-off frequencies of 0.1 and 9 MHz. However, acoustic distortions associated to speed of sound heterogeneities, acoustic scattering and attenuation as well as the response of the ultrasound sensing elements of the array are known to additionally play a role in the quality of the images rendered [61].

2.5. MRI

MRI scans were performed on a 7 T small animal MR Pharmascan (Bruker Biospin GmbH, Ettlingen, Germany) with a bore diameter of 16 cm and equipped with an actively shielded gradient capable of switching 760 mT□m with an 80 μs rise time and operated by a ParaVision 6.0 software platform (Bruker Biospin GmbH, Ettlingen, Germany). A circular polarized volume resonator was used for signal transmission, and an actively decoupled mouse brain quadrature surface coil with integrated combiner and preamplifier was used for signal receiving. Mice were anesthetized with an initial dose of 4% isoflurane (Abbott, Cham, Switzerland) in oxygen/air (200□800 mL□min) mixture and were maintained at 1.5 % isoflurane in oxygen/air (100□400 mL□min). Mice were next placed in prone position on a water-heated support to keep body temperature within 36.5 °C ± 0.5 °C, monitored with a rectal temperature probe. *In vivo* T_2-weighted MR images of mouse brain/head were obtained using a 2D spin echo sequence (Turbo rapid acquisition with refocused echoes) with imaging parameters: RARE factor 8, echo time 36 ms, repetition time 2628 ms, 6 averages, slice thickness 0.7 mm, no slice gap, field of view 20 mm × 20 mm, matrix 512 × 512, giving an in-plane spatial resolution 39 μm × 39 μm, out-of-plane resolution 0.7 mm (slice thickness), within a scan time 12 min 36 s.

2.6. Co-registration with MRI and VOI analysis of MSOT data

Registration between MSOT data and mouse brain MR images can provide a better anatomical reference for regional analysis. The cross-sectional MSOT images were co-registered with T_2 -weighted MRI data as described [62]. For dynamic data, time course of regional absorbance (a.u.) at 680 nm were plotted and the area-under-curves were calculated. The retention of probe was calculated by averaging values from 60−120 min post-injection.

2.7. Immunohistochemistry and confocal imaging

For immunohistochemistry and confocal microscopy, mice were perfused with 1 × PBS (pH 7.4), under ketamine/xylazine/acepromazine maleate anesthesia (75/10/2 mg/kg body weight, bolus injection) and decapitated. Brains were removed from the skull afterwards, fixed in 4 % paraformaldehyde in 1 × PBS (pH 7.4). Brain tissue were cut horizontally at 5 μm and stained with CRANAD-2, anti-$A\beta_{1-16}$ antibody 6E10 (Signet Lab, SIG-39320, 1:5000), fibrillar conformation anti-amyloid antibody OC (Merck, AB2286, 1:200), Donkey-anti-Rat Alexa 488 (Jackson, AB-2340686, 1:400), Goat-anti-Rabbit Alexa488 (Invitrogen, A11034, 1:200) and counter-stained using 4′,6-diamidino-2-phenylindole (DAPI) for nuclei (Sigma, D9542−10MG, 1:1000). Confocal images of the cortex of non-transgenic littermates and arcAβ mice were obtained using a Leica SP8 confocal microscope (Leica Microsystems GmbH, Germany) at ScopeM ETH Zurich Hönggerberg core facility. Sequential images were obtained by using 458 nm, 640 nm lines of the laser respectively. Identical settings were used and images were obtained for the non-transgenic littermates and arcAβ mice at ×20 and ×60 magnification, resolution with Z stack and maximum intensity projection.

2.8. Statistics

Unpaired two-tail *student t* test with Welch's correction was used (Graphpad Prism 8.2, Graphpad Software Inc, USA) for comparing values between arcAβ mice and non-transgenic littermates. All data are present as mean ± standard deviation. Significance was set at * $p < 0.05$.

3. Results

3.1. In vitro characterization of probes on recombinant $A\beta_{1-42}$ fibrils

We performed a fluorescence assay to assess the binding of CRANAD-2 to pre-formed $A\beta_{1-42}$ fibrils (Fig. 1) and compared CRANAD-2 with the Thioflavin T (ThT) dye, a small molecule which increases fluorescence signal upon binding to amyloids and currently represents the most common probe for *in vitro* assay of amyloid formation [63]. As expected, ThT binding to $A\beta_{1-42}$ fibrils (0−0.2 μM), resulted in a dose-dependent increase in fluorescence intensities at 484 nm (Figs. 1a-c). Upon binding to $A\beta_{1-42}$ fibrils, CRANAD-2 showed a similar dose-dependent increase in fluorescence intensity at 681 nm (Figs. 1d-f). Linear relations between fluorescence intensity and concentration of 0−0.2 μM and 0−0.012 μM $A\beta_{1-42}$ fibrils were observed both with CRANAD-2 (Fig. 1e, $p = 1 \times 10^{-12}$, $r^2 = 0.991$; Fig. 1f, $p = 0.0015$, $r^2 = 0.9831$) and ThT (Fig. 1b, $p =$

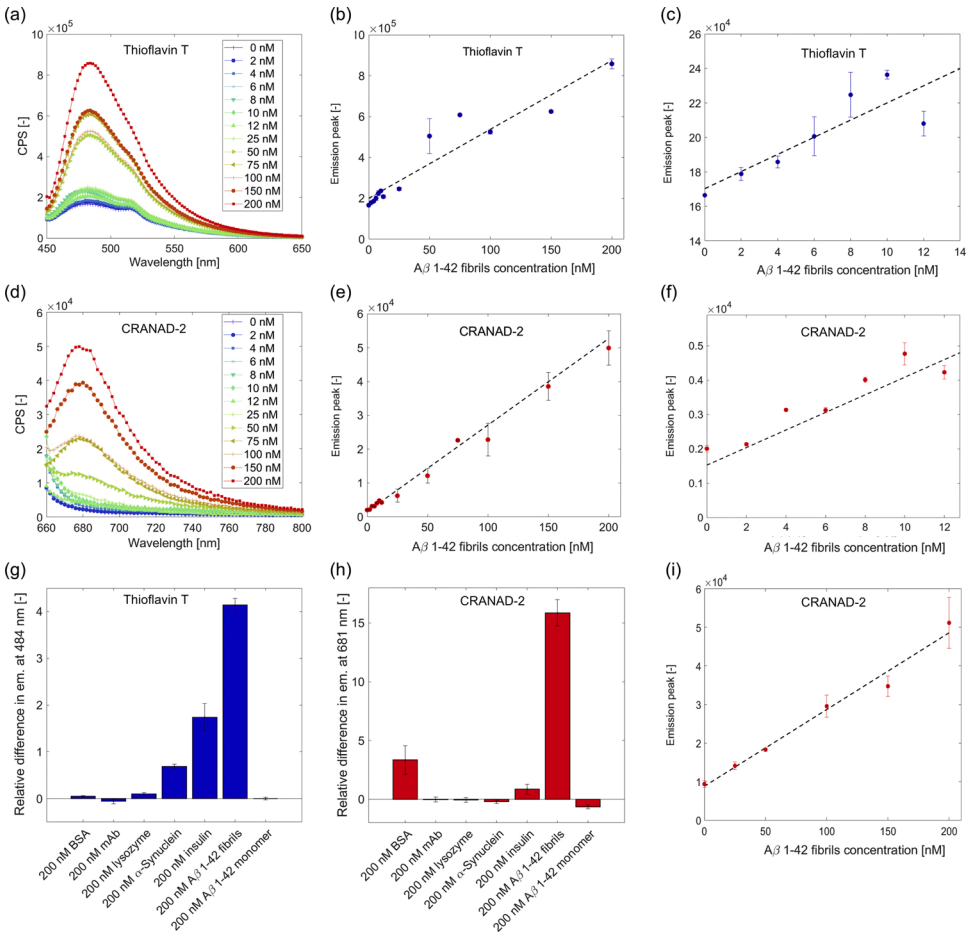

Fig. 1. ***In vitro*** **characterization of CRANAD-2 binding to recombinant Aβ$_{1\text{-}42}$ fibrils.** (**a-f**) Fluorescence intensity spectrum (counts per seconds, CPS) of recombinant Aβ$_{1\text{-}42}$ fibrils (0-0.2 μM) in the presence of 20 μM ThT (**a**) and 0.1 μM CRANAD-2 (**d**); (**b-c**) Linear relation between signal at emission peak of ThT (484 nm) and Aβ$_{1\text{-}42}$ fibrils concentration in the range of 0-0.2 μM (**b**) and 0-0.012 μM (**c**); (**e-f**) Linear relation between emission peak of CRANAD-2 (681 nm) and Aβ$_{1\text{-}42}$ fibrils concentration in the range of 0-0.2 μM (**e**) and 0-0.012 μM (**f**); (**g-i**) Comparison of ThT (**g**) and CRANAD-2 (**h**) binding to different proteins. (**i**) Linear relation of the fluorescence intensity of CRANAD-2 as function of Aβ$_{1\text{-}42}$ fibrils spiked in a cell lysate; In panels b, c, e, f, g, h, and i, error bars represent standard deviations corresponding to 3 independent measurements. BSA: bovine serum albumin; mAb: monoclonal antibody; Data are shown as mean ± standard deviation. Statistical test; $p < 0.05$.

4×10^{-7}, $r^2 = 0.9155$; Fig. 1c, $p = 0.0136$, $r^2 = 0.7352$), respectively.

In a second set of experiments, we assessed the binding of CRANAD-2 and ThT to other proteins, including monomeric proteins rich in β-sheet structures, amyloid fibrils composed of other proteins and monomeric Aβ$_{1-42}$ peptide. ThT showed high intensity upon binding to Aβ$_{1-42}$ fibrils and a lower intensity when incubated with α-synuclein, and insulin (Fig. 1g).

CRANAD-2 showed higher intensity signal upon binding to Aβ$_{1-42}$ fibrils compared to fibrils composed of α-synuclein, insulin, lysosome, and to the Aβ$_{1-42}$ monomer, while a non-negligible signal was observed in the presence of bovine serum albumin (Fig. 1h). Compared to CRANAD-2, the signal intensity of ThT upon binding to fibrils of α-synuclein and insulin was higher (Fig. 1g), indicating that the fluorescence signal of CRANAD-2 is more specific to Aβ$_{1-42}$ fibrils and a less generic report of the presence of β-sheet structures.

We further investigated the specificity of CRANAD-2 (0.1 μM) for Aβ$_{1-42}$ fibrils (0−0.2 μM) by performing the same assay in a complex sample represented by a cell lysate with estimated total protein concentration of 7 μM. Notably, a linear relationship between Aβ$_{1-42}$ fibrils and CRANAD-2 fluorescence intensity was observed, even when fibrils were spiked in a cell lysate containing a much higher concentration of a variety of proteins (Fig. 1i).

Overall, these results demonstrate that CRANAD-2 can bind Aβ$_{1-42}$ fibrils with high affinity and specificity, even in complex mixtures. Importantly, the probe can distinguish between monomeric and fibrillar forms of the peptide.

3.2. In vitro binding of CRANAD-2 to Aβ fibrils increases fluorescence but not OA signal

CRANAD-2 was incubated with Aβ fibrils and measured using an agar phantom with vMSOT and epifluorescence imaging (Fig. 2c, d, SFig. 1). We have extracted the absorbance of CRANAD-2 from the vMSOT measurement and show its absorption spectrum along with the absorbance spectrum of Hb and HbO [64] (Fig. 2a). In addition, we obtained the fluorescence excitation and emission spectrum of CRANAD-2 with a spectrofluorometer (Fig. 2a, b). Analysis of vMSOT images of the phantom did not show a difference in OA signal when CRANAD-2 was co-incubated with Aβ fibrils compared to CRANAD-2 alone (Fig. 2e). In contrast, co-incubation of CRANAD-2 with Aβ fibrils did result in a 50 % increase in fluorescence intensity compared to CRANAD-2 alone (Fig. 2f).

3.3. In vivo hybrid vMSOT and epi-fluorescence imaging in arcAβ mouse brain

CRANAD-2 has been shown to cross the blood-brain-barrier and reach the brain parenchyma [33,34]. We explored the ability of OA imaging to detect Aβ deposits *in vivo* in mouse brain. We used a hybrid system to assess simultaneous 3D vMSOT and planar epi-fluorescence imaging for CRANAD-2 distribution in arcAβ mouse brain. Two arcAβ mouse was scanned *in vivo* using the hybrid system with intact scalp till 120 min after CRANAD-2 probe injection. A volumetric image is obtained with vMSOT is shown (Figs. 3 and 4). We did not attain actual unmixing of CRANAD-2 and deoxy/oxyhemoglobin (Hb/HbO) signal probably due to the low concentration of probe in the tissue compared to the other two absorbers. We consider endogenous Hb and HbO represent

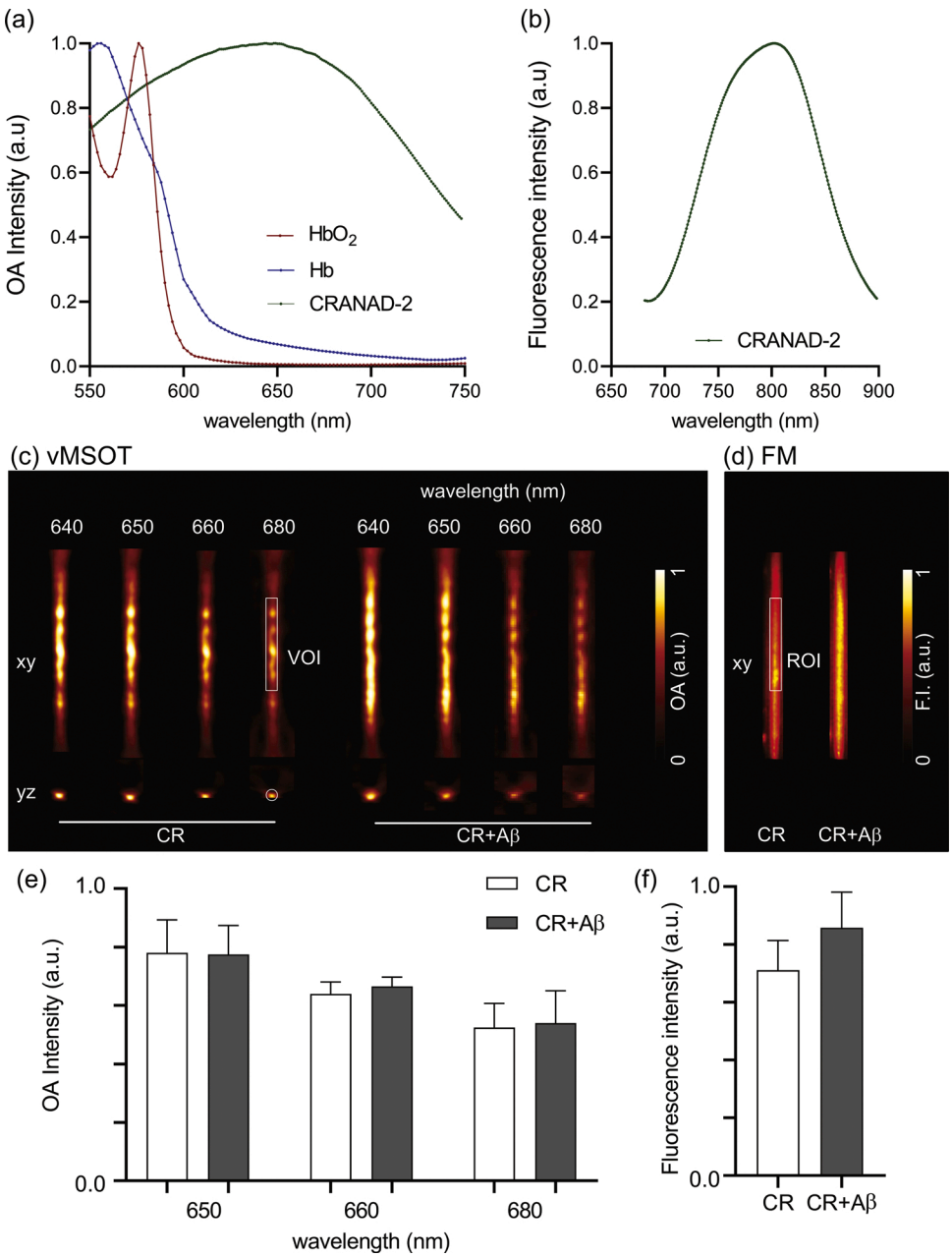

Fig. 2. ***In vitro*** **hybrid 3D vMSOT and epi-fluorescence imaging of CRANAD-2 and Aβ fibrils.** One tubing was fixed on agar support platform was filled with samples containing CRANAD-2 (1 μM) with and without Aβ (1 μM), and measured by using 3D hybrid vMSOT epi-fluorescence microscopy system; (**a**) Absorbance of CRANAD-2 unmixed from measurement shown along with the absorbance spectrum of deoxyhemoglobin (Hb), and oxyhemoglobin (HbO) [64]; (**b**) Fluorescence emission spectrum of CRANAD-2 (25 μM in PBS, pH7.4) measured using a spectrofluorometer; (**c**) vMSOT measured signal at multiple wavelengths (640-680 nm) and (**d**) fluorescence signal from the tubing; (**e**) Quantification of optoacoustic signal intensity at different wavelengths in shown in the VOI shown in the white box in (**a**); (**f**) Quantification of fluorescence signal shown in the VOI shown in the white box in (**b**). Data is shown as mean ± SD; CR: CRANAD-2.

the OA signal intensity at preinjection (Fig. 4c), which is much abundant compared to the increase in OA signal intensity caused by the injection of CRANAD-2, Changes in MSOT signal (660–850 nm wavelength, acquired with 5 nm gap) in the arcAβ mouse brain were also monitored (Fig. 3). Signal was mainly observed in cortical structures. We observed minor difference between 660 and 680 nm, which fits with the absorbance spectrum of CRANAD-2 with rather flat decline in the absorbance intensity with increase of wavelength.

3.4. *MSOT detects Aβ deposits in vivo*

Based on the results in section 3.3., we next set out to explore the ability of 3D whole brain Aβ mapping with a commercial MSOT system with 2D image acquisition and 0.3 mm gap between slides. This system cover the spectrum range of 680−850 nm. To allow for accurate regional analysis, we register the MSOT data with MRI data which provides better soft tissue contrast (Fig. 5, SFig. 2). We monitored CRANAD-2 uptake in arcAβ mice and non-transgenic littermates for 90 min post-injection (n = 3–4 each) (Figs. 5a-c). The delta images in relation to the pre-injection images shows high probe uptake in the brain of arcAβ mice, mainly in the cortex (Fig. 5c). Analysis of the dynamics of cortical CRANAD-2 uptake allowed to discriminate arcAβ mice from non-transgenic littermates (Fig. 5a, d). The signal plateaued around 90 min. Higher AUC was observed in the cortical region of arcAβ mice compared to non-transgenic littermates (Fig. 5e).

3.5. *Ex vivo staining on mouse brain sections*

To validate the specificity of CRANDA-2 binding to Aβ deposits in mouse brain, horizontal brain tissue sections from arcAβ mice and non-transgenic littermates were stained with CRANAD-2 in addition to anti-Aβ antibodies 6E10, which binds any type of Aβ, and OC, which recognizes mature fibrils [65], and were nuclear counterstained with DAPI (Fig. 6). No signal was observed in the cortex from non-transgenic littermates (Figs. 6a, f). CRANAD-2 clearly co-stained with OC or 6E10 stained parenchymal and vessel-associated Aβ deposits in the arcAβ

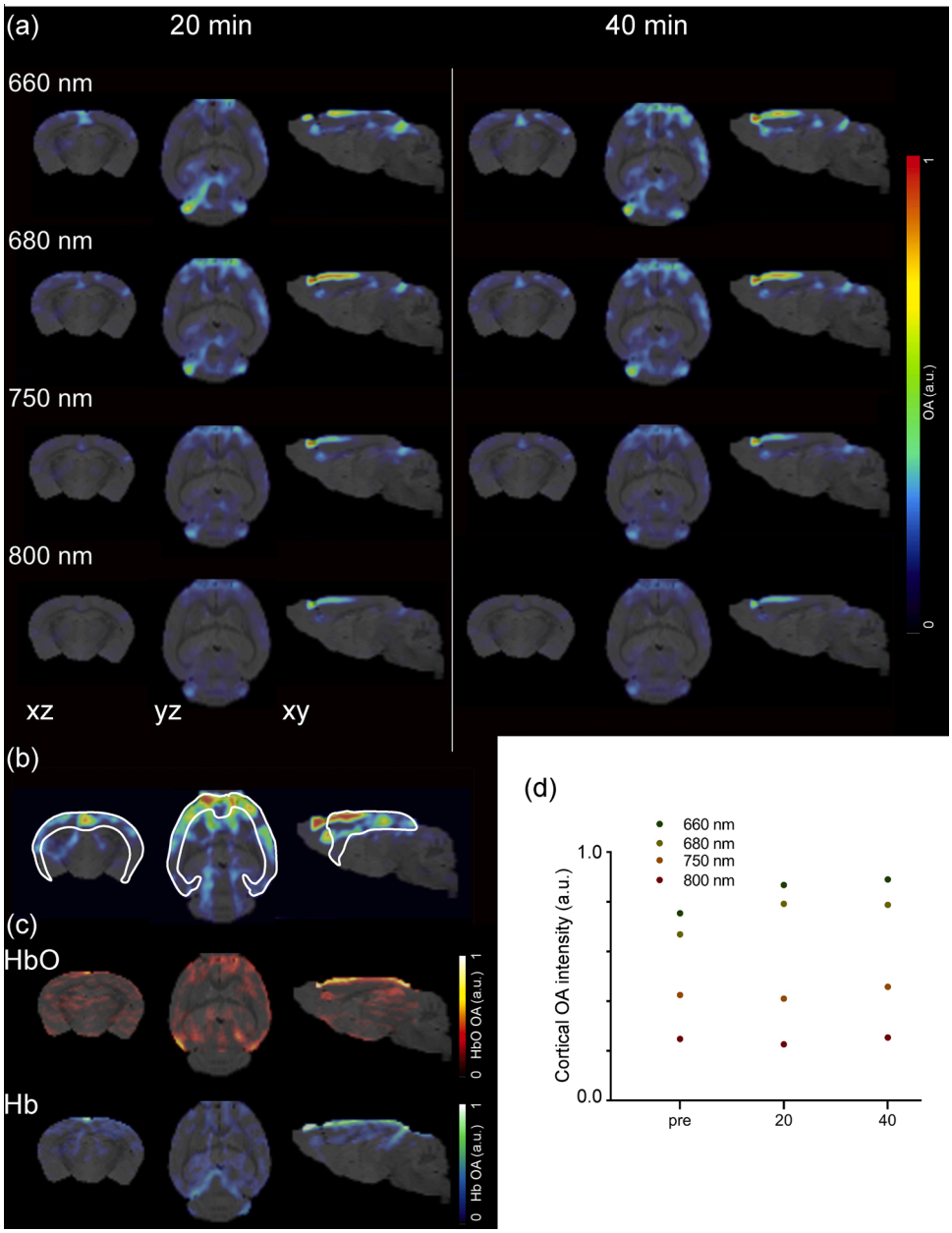

Fig. 3. ***In vivo*** **3D vMSOT imaging of CRANAD-2 in an arcAβ mouse. (a)** vMSOT 3D volumetric images at 660, 680, 750, 800 nm (horizontal, sagittal and coronal views) are shown respectively; at 20 and 40 min post-injection of CRANAD-2; (**b**) Illustration of VOI analysis of cortical region; (**c**) 3D volumetric images of hemoglobin (HbO) and deoxyhemoblin (Hb) at preinjection; (**d**) Optoacoustic (OA) signal intensity at 660, 680, 750, and 800 nm at different time points.

mouse brain (Fig. 6b-e, g-n). This suggests specific binding of CRANAD-2 to Aβ deposits. We also observed auto-fluorescence (blue) of Aβ plaques in the cortical region of arcAβ mouse brain tissue slice (Fig. 6o), similar to other reports [66].

4. Discussion

Developing tools for non-invasive detection of Aβ deposits at high-resolution in animal models of AD is critical for investigating disease mechanism and translational development of Aβ-targeted therapies. Most probes for Aβ including NIAD-4 [25], AOI-987 [26], BODIPY [27], THK-265 [28], DANIR [29–32], curcumin-derivatives CRANAD series [33,34], luminescent conjugated oligothiophenes [35,36] and DBA-SLOH [37] have been so far been designed for fluorescence imaging application. Nevertheless, Aβ binding fluorescent probes with suitable absorbance spectrum can be employed for OA imaging. We took advantage of the fluorescent property of CRANAD-2 to characterize the suitable of the probe to map cerebral Aβ deposits with NIRF and OA imaging.

The detection sensitivity is higher in PET compared to optical and optoacoustic imaging. Depending on the probe affinity, detection of nanomolar concentration of probes have been reported [67–69]. Whereas in optoacoustic imaging, higher concentrations of probe are needed to achieve detectable signal. The resolution of PET for small animal is usually 0.7–1.5 mm which is almost 10 times lower than that of optoacoustic imaging. In microPET the partial volume effect influence the accuracy of the quantification due to the size of the mouse brain.

CRANAD-2 has an affinity to Aβ aggregates of 0.0387 μM [33], which is much higher than those of BODIPY, AOI-987 [26], similar to DANIR [32] and lower than NIAD-4 [25,32]. The *in vitro* binding assay demonstrated a linear relationship between fluorescence intensity and concentration of aggregated $A\beta_{1-42}$ fibrils for CRANAD-2. This

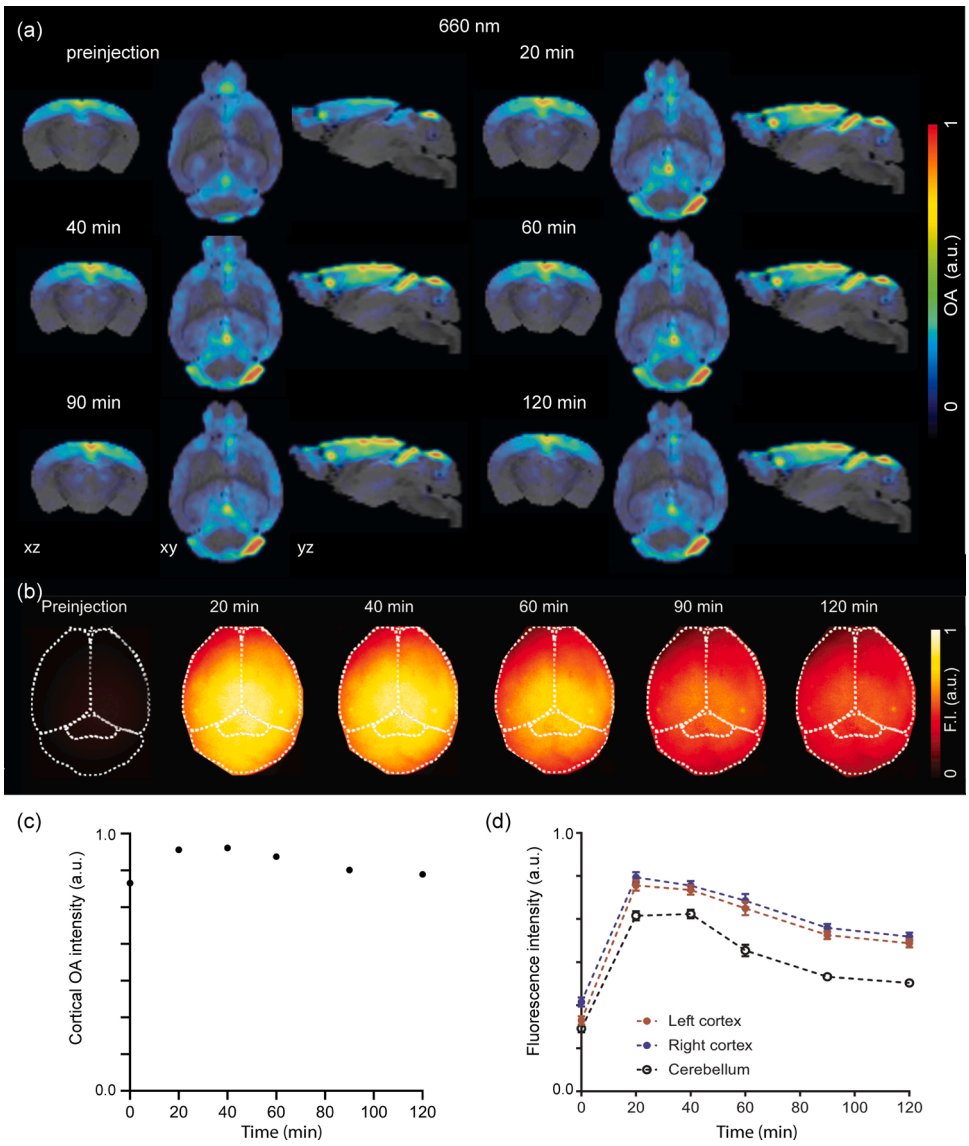

Fig. 4. ***In vivo*** **hybrid 3D vMSOT and epifluorescence imaging of CRANAD-2 in an arcAβ mouse.** (**a**) vMSOT 3D volumetric images at 660 nm (horizontal, sagittal and coronal views) are shown respectively; at pre-injection, 20 to 120 min post-injection of CRANAD-2; (**b**) Epi-fluorescence (horizontal view) (**c**) Optoacoustic (OA) signal intensity at 660 nm and (**d**) Fluorescence signal as a function of time in the right and left cortex and compared to cerebellum of an arcAβ mouse.

properties has been reported for many Aβ binding probes such as AOI-987, THK-265, DANIR and croconium dye [26,28,32,45] and constitutes an advantage for the detection of fluorescence in NIRF imaging. However, when applying such probes for MSOT imaging, the increase in fluorescence quantum yield upon Aβ binding is expected to lead to a decrease in MSOT signal. Despite this feature, two previous studies in a transgenic mouse model of amyloidosis have reported Aβ imaging with other optoacoustic imaging systems using Congo Red [27], and croconium dye [45]. We were also able to clearly detect optoacoustic signals from CRANAD-2 bound to Aβ fibrils in the phantom and in arcAβ mice *in vivo*. Moreover, there were no differences in OA signal between CRANAD-2 to recombinant Aβ fibrils and CRANAD-2 alone measured in the phantom with MSOT. In addition to an increase in fluorescence intensity, we observed a slight red-shift by 75 nm in fluorescence spectrum upon binding to aggregated $A\beta_{1-42}$ fibrils as describes in previous reports [33]. Importantly, the probe exhibits little binding to other proteins involved with Aβ plaque formation such as lysozyme [70]. Though, we observed a percentage of binding to bovine serum albumin that is a plasma protein in the circulation and found in Aβ plaques. This is a common phenomenon of Aβ binding probes such as BTA-1, PIB, florbetaben, florbetapir *etc* [71–74]. Co-staining of CRANAD-2 to brain sections from arcAβ mice with 6E10/OC antibodies of Aβ deposition clearly showed close resemblance in both vascular and parenchymal Aβ deposits.

CRANAD-2 is well-characterized since the development in 2009 [30,33,34]. In our study (Fig. 1), we characterized the binding properties of probe *in vitro* and showed specific binding to amyloid-β fibril compared to other proteins such as a-synuclein and insulin. There is minor binding to albumin which is common for most of the Aβ probes such as PIB, florbetaben *etc.* Moreover, we demonstrated in Fig. 6 with immunohistochemistry that CRANAD-2 specifically binds to Aβ plaques. Given the specificity of CRANAD-2 for Aβ deposits and the fact that the probe generates a detectable MSOT signal upon Aβ fibril binding, we explored the capability of *in vivo* MSOT cerebral Aβ mapping. Probes for MSOT imaging ideally have an absorbance and emission peak at NIR or even NIR II range to allow for sufficient penetration depth and separation from deoxygenated and oxygenated hemoglobin which are abundant in biological tissue, but which have lower absorption in the NIR region of light [19]. This has been considered in the design of most Aβ probes, apart from NIAD-4 and Congo Red which have absorption peaks in the

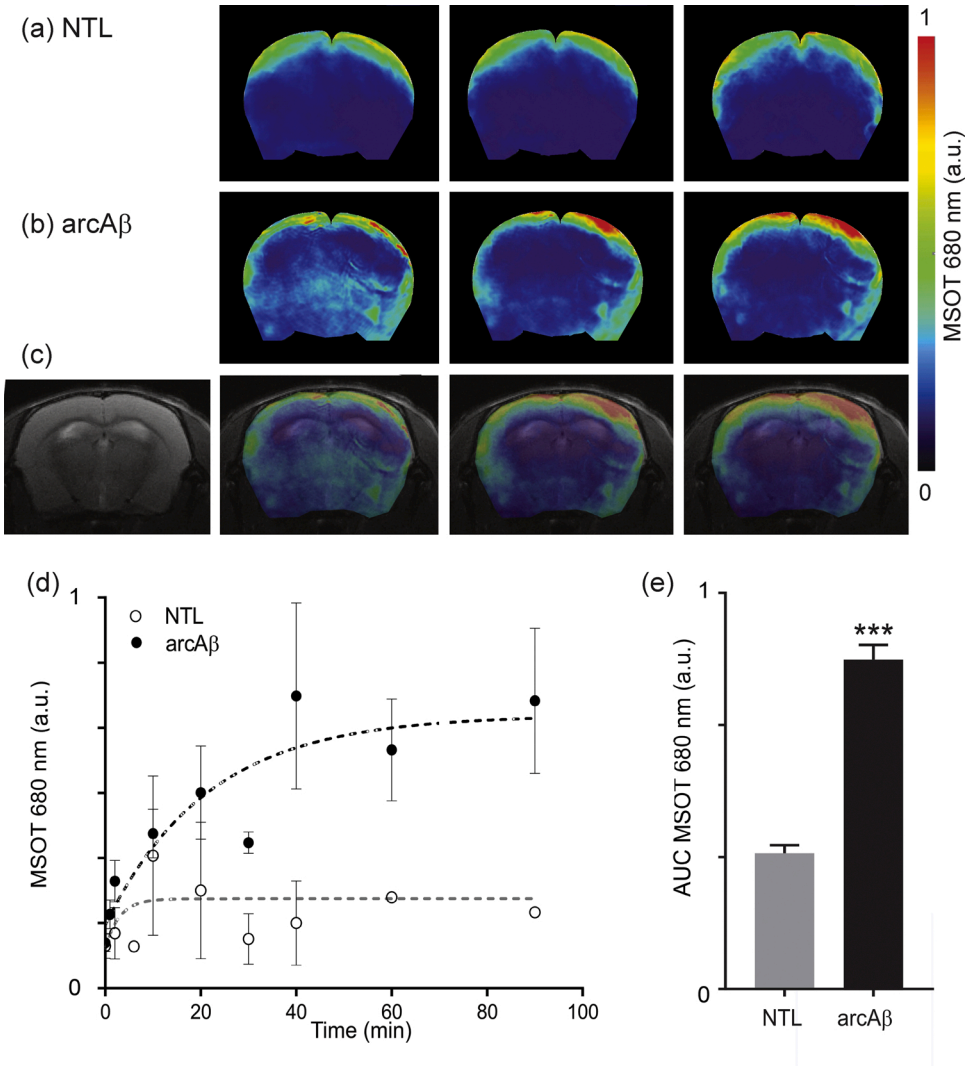

Fig. 5. *In vivo* planar MSOT imaging of CRANAD-2 in mouse models. (**a, b**) Coronal view of optoacoustic images of a non-transgenic littermate and an arcA**β** mouse; (**c**) a T_2-weighted structural MR image and optoacoustic images of arcA**β** mice overlaid with structural MR image at 680 nm at 10, 40 and 90 min after *i.v.* tail vein injection of CRANAD-2; The MSOT system acquire 2D images (with 0.3 mm gap between each scan, the holder moving along the axis from anterior to posterior position); (**d**) Time course of MOST intensity at 680 nm in the cortex of NTL (non-transgenic littermates) and arcA**β** mice over 120 min; (**e**) Quantification of area-under-curve (AUC) in NTL and arcA**β** mice. Data are shown as mean ± standard deviation; ***$p < 0.05$.

red part of the spectrum and which require invasive imaging approaches [25]. Moreover, some probes, *e.g.* BODIPY [27] derivatives and Congo red [27], do not pass across the blood-brain barrier and thus have to be injected intrathecally. CRANAD-2 has a suitable spectrum (excitation maximum 640 nm, emission maximum 685 nm) [33]. In previous reports it was shown that CRANAD-2 passes the blood-brain barrier [33,34]. This has motivated us to inject the probe in arcAβ mice, which shows parenchymal plaque and cerebral amyloid angiopathy accumulation concomitantly with cognitive impairments from 6 months-of-age, where Aβ plaque load increases with age [46].

The optical absorption and fluorescence contrast provided by CRANAD-2 allowed for cross-validation by simultaneous real-time recording of hybrid 3D vMSOT and 2D epi-fluorescence data [57], useful to understand the relation between the fluorescence, absorbance and spectral dependence of the signals generated from probe binding to targets [75]. We observed uptake and wash-out of probe with MSOT and epi-fluorescence imaging, though the degree of changes in MSOT signal was lower. The differences may be explained by the fact that epi-fluorescence lacks the depth resolving capacity. Thus effectively signals originating from different cranial compartments (skull and scalp over the head) adds up to provide a surface-weighted signal [76]. In contrast, tomographic MSOT imaging allows to map the probe uptake in the brain more accurately in 3D. Thus, epi-fluorescence imaging merely reflects a mixture of wash-out kinetics from different tissues, while MSOT closer represents the actual cerebral kinetics.

We did not attain actual unmixing of CRANAD-2 (probably due to the low concentration of probe in the brain). [30,34] Injecting a higher amount of probe might help but is limited by the rather low solubility of the probe in water. In addition, using more wavelengths could also potentially help during the data acquisition.

To harness the full potential of volumetric imaging, we performed serial MSOT imaging in arcAβ and non-transgenic littermates. Co-registration of MSOT data with a T_2-weighted structural MRI dataset [44,62] allowed to quantify regional probe uptake. We observed a clear difference in brain accumulation of CRANAD-2. In our study, the cortical signals detected by using epi-fluorescence imaging and vMSOT in arcAβ mice in this study was in accordance with the known Aβ distribution, which is highest in dorsal areas like the cortex and decreases ventrally [43,46,49], and the validation from immunohistochemistry. Several factors influence the image quality of MSOT, such as the modeling accuracy of light propagation in living tissues [77]. Further application of regional based fluence correction and non-negative correction in the reconstruction and unmixing steps will enable more accurate quantification [78,79].

In conclusion, we demonstrated the suitability of CRANAD-2 for detecting Aβ deposits in a mouse model of AD amyloidosis with epi-fluorescence and MSOT imaging. The approach offers further longitudinal monitoring of therapeutics effect targeting at Aβ and for unveiling the disease mechanism in animal models.

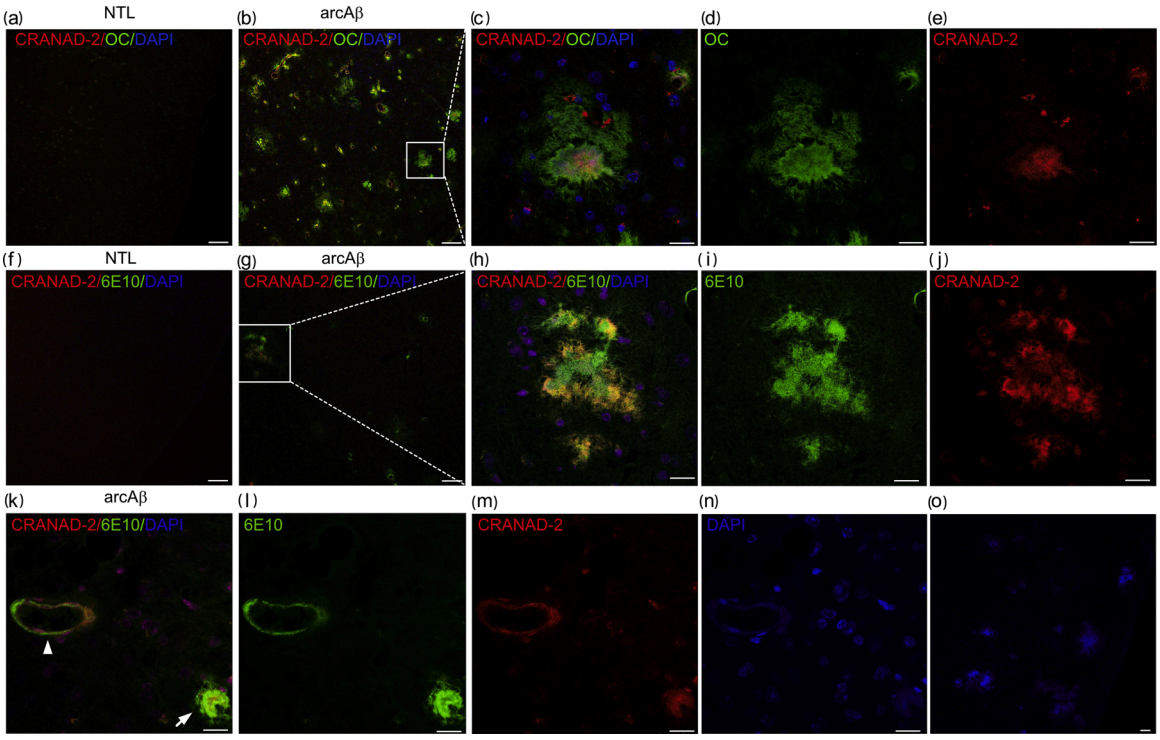

Fig. 6. Co-staining of CRANAD-2 with Aβ deposition in non-transgenic littermate and arcAβ mouse brain tissue sections. Sections were stained with CRANAD-2 (red) and fibrillar conformation antibody OC (green) and anti-$A\beta_{1-16}$ antibody 6E10 (green), and DAPI (blue) in the cortex of non-transgenic littermates (NTL) (**a, f**) and arcAβ mice (**b, g**); (**c-e, h-j**) zoom-in illustrating co-localization of the signal in (**b, g**); (**k-n**) Vessel associated cerebral amyloid angiopathy (arrowhead) and parenchymal plaque (arrow); (**o**) Autofluorescnce of Aβ plaques in the cortex of arcAβ mouse in the absence of stainings; Scale bars = 50 μm (**a, b, f, g**), 20 μm (**c-e, h-o**) (For interpretation of the references to colour in this figure legend, the reader is referred to the web version of this article).

Funding

JK received funding from the Swiss National Science Foundation (320030_179277), in the framework of ERA-NET NEURON (32NE30_173678/1), Vontobel foundation, Olga Mayenfisch Stiftung, and the Synapsis foundation. RN received funding from Synapsis foundation career development award (2017 CDA-03), Helmut Horten Stiftung and Jubiläumsstiftung von Swiss Life, UZH Entrepreneur Fellowship of the University of Zurich, reference no. [MEDEF-20−021]. PA acknowledges financial support from the Synapsis foundation. Funding from the European Research Council (grant number ERC-CoG-2015-682379) to DR is also acknowledged.

Availability of data and material

The datasets generated and/or analyzed during the current study are available in the repository DOI zenodo: https://doi.org/10.5281/zenodo.3672403.

Author contributions

RN, AV, PA and JK conceived and designed the study; RN, AV, XD, ZC performed the experiments; RN, AV, XD, ZC, PA analyzed the data; RN, AV, XD, ZC, PA, JK interpreted the results; RN, AV and JK wrote the initial paper draft; all coauthors contributed constructively to writing and editing the manuscript.

Declaration of Competing Interest

The authors declare that there are no conflicts of interest.

Acknowledgement

The authors acknowledge support from Michael Reiss, Marie Rouault at Institute for Biomedical Engineering, ETH & University of Zurich; Daniel Schuppli at Institute for Regenerative Medicine, University of Zurich; Dr. Joachim Hehl of the Scientific Center for Optical and Electron Microscopy (ScopeM) of ETH Zurich.

Appendix A. Supplementary data

Supplementary material related to this article can be found, in the online version, at doi:https://doi.org/10.1016/j.pacs.2021.100285.

References

[1] J. Hardy, D.J. Selkoe, The amyloid hypothesis of Alzheimer's disease: progress and problems on the road to therapeutics, Science 297 (5580) (2002) 353–356.
[2] R. Riek, D.S. Eisenberg, The activities of amyloids from a structural perspective, Nature 539 (7628) (2016) 227–235.
[3] C.R. Jack Jr., D.A. Bennett, K. Blennow, M.C. Carrillo, B. Dunn, S.B. Haeberlein, D. M. Holtzman, W. Jagust, F. Jessen, J. Karlawish, E. Liu, J.L. Molinuevo, T. Montine, C. Phelps, K.P. Rankin, C.C. Rowe, P. Scheltens, E. Siemers, H.M. Snyder, R. Sperling, NIA-AA Research Framework: toward a biological definition of alzheimer's disease, Alzheimers Dement. 14 (4) (2018) 535–562.
[4] C.M. Clark, J.A. Schneider, B.J. Bedell, T.G. Beach, W.B. Bilker, M.A. Mintun, M. J. Pontecorvo, F. Hefti, A.P. Carpenter, M.L. Flitter, M.J. Krautkramer, H.F. Kung, R.E. Coleman, P.M. Doraiswamy, A.S. Fleisher, M.N. Sabbagh, C.H. Sadowsky, E. P. Reiman, S.P. Zehntner, D.M. Skovronsky, Use of florbetapir-PET for imaging beta-amyloid pathology, Jama 305 (3) (2011) 275–283.
[5] O. Sabri, M.N. Sabbagh, J. Seibyl, H. Barthel, H. Akatsu, Y. Ouchi, K. Senda, S. Murayama, K. Ishii, M. Takao, T.G. Beach, C.C. Rowe, J.B. Leverenz, B. Ghetti, J. W. Ironside, A.M. Catafau, A.W. Stephens, A. Mueller, N. Koglin, A. Hoffmann, K. Roth, C. Reininger, W.J. Schulz-Schaeffer, G. Florbetaben, Phase 3 Study, Florbetaben PET imaging to detect amyloid beta plaques in Alzheimer's disease: phase 3 study, Alzheimers Dement. 11 (8) (2015) 964–974.
[6] C. Curtis, J.E. Gamez, U. Singh, C.H. Sadowsky, T. Villena, M.N. Sabbagh, T. G. Beach, R. Duara, A.S. Fleisher, K.A. Frey, Z. Walker, A. Hunjan, C. Holmes, Y. M. Escovar, C.X. Vera, M.E. Agronin, J. Ross, A. Bozoki, M. Akinola, J. Shi, R. Vandenberghe, M.D. Ikonomovic, P.F. Sherwin, I.D. Grachev, G. Farrar, A.

P. Smith, C.J. Buckley, R. McLain, S. Salloway, Phase 3 trial of flutemetamol labeled with radioactive fluorine 18 imaging and neuritic plaque density, JAMA Neurol. 72 (3) (2015) 287–294.
[7] V.L. Villemagne, V. Dore, S.C. Burnham, C.L. Masters, C.C. Rowe, Imaging tau and amyloid-beta proteinopathies in Alzheimer disease and other conditions, Nat. Rev. Neurol. 14 (4) (2018) 225–236.
[8] W.E. Klunk, H. Engler, A. Nordberg, Y. Wang, G. Blomqvist, D.P. Holt, M. Bergstrom, I. Savitcheva, G.F. Huang, S. Estrada, B. Ausen, M.L. Debnath, J. Barletta, J.C. Price, J. Sandell, B.J. Lopresti, A. Wall, P. Koivisto, G. Antoni, C. A. Mathis, B. Langstrom, Imaging brain amyloid in Alzheimer's disease with Pittsburgh Compound-B, Ann. Neurol. 55 (3) (2004) 306–319.
[9] E. Rodriguez-Vieitez, R. Ni, B. Gulyas, M. Toth, J. Haggkvist, C. Halldin, L. Voytenko, A. Marutle, A. Nordberg, Astrocytosis precedes amyloid plaque deposition in Alzheimer APPswe transgenic mouse brain: a correlative positron emission tomography and in vitro imaging study, Eur. J. Nucl. Med. Mol. Imaging 42 (7) (2015) 1119–1132.
[10] A. Rominger, M. Brendel, S. Burgold, K. Keppler, K. Baumann, G. Xiong, E. Mille, F. J. Gildehaus, J. Carlsen, J. Schlichtiger, S. Niedermoser, B. Wangler, P. Cumming, H. Steiner, J. Herms, C. Haass, P. Bartenstein, Longitudinal assessment of cerebral beta-amyloid deposition in mice overexpressing Swedish mutant beta-amyloid precursor protein using 18F-Florbetaben PET, journal of nuclear medicine : official publication, Indian J. Nucl. Med. 54 (7) (2013) 1127–1134.
[11] D. Sehlin, X.T. Fang, L. Cato, G. Antoni, L. Lannfelt, S. Syvanen, Antibody-based PET imaging of amyloid beta in mouse models of Alzheimer's disease, Nat. Commun. 7 (2016) 10759.
[12] F.C. Maier, H.F. Wehrl, A.M. Schmid, J.G. Mannheim, S. Wiehr, C. Lerdkrai, C. Calaminus, A. Stahlschmidt, L. Ye, M. Burnet, D. Stiller, O. Sabri, G. Reischl, M. Staufenbiel, O. Garaschuk, M. Jucker, B.J. Pichler, Longitudinal PET-MRI reveals beta-amyloid deposition and rCBF dynamics and connects vascular amyloidosis to quantitative loss of perfusion, Nat. Med. 20 (12) (2014) 1485–1492.
[13] H. Hong, L. Zhang, F. Xie, R. Zhuang, D. Jiang, H. Liu, J. Li, H. Yang, X. Zhang, L. Nie, Z. Li, Rapid one-step 18F-radiolabeling of biomolecules in aqueous media by organophosphine fluoride acceptors, Nat. Commun. 10 (1) (2019) 989.
[14] Z. Li, X. Zhang, X. Zhang, M. Cui, J. Lu, X. Pan, X. Zhang, (18)F-Labeled benzyldiamine derivatives as novel flexible probes for positron emission tomography of cerebral β-Amyloid plaques, J. Med. Chem. 59 (23) (2016) 10577–10585.
[15] H. Fu, Z. Chen, L. Josephson, Z. Li, S.H. Liang, Positron emission tomography (PET) ligand development for ionotropic glutamate receptors: challenges and opportunities for radiotracer targeting N-Methyl-d-aspartate (NMDA), α-Amino-3-hydroxy-5-methyl-4-isoxazolepropionic acid (AMPA), and kainate receptors, J. Med. Chem. 62 (2) (2019) 403–419.
[16] E. Brown, J. Brunker, S.E. Bohndiek, Photoacoustic imaging as a tool to probe the tumour microenvironment, Dis. Model. Mech. 12 (7) (2019).
[17] X.L. Deán-Ben, S. Gottschalk, B. Mc Larney, S. Shoham, D. Razansky, Advanced optoacoustic methods for multiscale imaging of in vivo dynamics, Chem. Soc. Rev. 46 (8) (2017) 2158–2198.
[18] S.V. Ovsepian, I. Olefir, G. Westmeyer, D. Razansky, V. Ntziachristos, Pushing the boundaries of neuroimaging with optoacoustics, Neuron 96 (5) (2017) 966–988.
[19] J. Klohs, A. Wunder, K. Licha, Near-infrared fluorescent probes for imaging vascular pathophysiology, Basic Res, Cardiol. 103 (2) (2008) 144–151.
[20] D. Razansky, J. Klohs, R. Ni, Multi-scale optoacoustic molecular imaging of brain diseases, Eur. J. Nucl. Med. Mol. Imaging (2021).
[21] Y. Liu, Y. Yang, M. Sun, M. Cui, Y. Fu, Y. Lin, Z. Li, L. Nie, Highly specific noninvasive photoacoustic and positron emission tomography of brain plaque with functionalized croconium dye labeled by a radiotracer, Chem. Sci. 8 (4) (2017) 2710–2716.
[22] W. Li, R. Chen, J. Lv, H. Wang, Y. Liu, Y. Peng, Z. Qian, G. Fu, L. Nie, In vivo photoacoustic imaging of brain injury and rehabilitation by high-efficient near-infrared dye labeled mesenchymal stem cells with enhanced brain barrier permeability, Adv. Sci. Weinh. (Weinh) 5 (2) (2018), 1700277.
[23] Y. Liu, H. Liu, H. Yan, Y. Liu, J. Zhang, W. Shan, P. Lai, H. Li, L. Ren, Z. Li, L. Nie, Aggregation-induced absorption enhancement for deep near-infrared II photoacoustic imaging of brain gliomas in vivo, Adv. Sci. 6 (8) (2019), 1801615.
[24] K.J. Cao, J. Yang, Translational opportunities for amyloid-targeting fluorophores, Chem. Commun. (Camb.) 54 (66) (2018) 9107–9118.
[25] E.E. Nesterov, J. Skoch, B.T. Hyman, W.E. Klunk, B.J. Bacskai, T.M. Swager, In vivo optical imaging of amyloid aggregates in brain: design of fluorescent markers, Angew. Chem. Int. Ed. Engl. 44 (34) (2005) 5452–5456.
[26] M. Hintersteiner, A. Enz, P. Frey, A.L. Jaton, W. Kinzy, R. Kneuer, U. Neumann, M. Rudin, M. Staufenbiel, M. Stoeckli, K.H. Wiederhold, H.U. Gremlich, In vivo detection of amyloid-beta deposits by near-infrared imaging using an oxazine-derivative probe, Nat. Biotechnol. 23 (5) (2005) 577–583.
[27] M. Ono, H. Watanabe, H. Kimura, H. Saji, BODIPY-based molecular probe for imaging of cerebral β-amyloid plaques, ACS Chem, Neurosci. 3 (4) (2012) 319–324.
[28] N. Okamura, M. Mori, S. Furumoto, T. Yoshikawa, R. Harada, S. Ito, Y. Fujikawa, H. Arai, K. Yanai, Y. Kudo, In vivo detection of amyloid plaques in the mouse brain using the near-infrared fluorescence probe THK-265, J. Alzheimers Dis. 23 (1) (2011) 37–48.
[29] C. Ran, W. Zhao, R.D. Moir, A. Moore, Non-conjugated small molecule FRET for differentiating monomers from higher molecular weight amyloid beta species, PLoS One 6 (4) (2011), e19362.
[30] J. Yang, X. Zhang, P. Yuan, J. Yang, Y. Xu, J. Grutzendler, Y. Shao, A. Moore, C. Ran, Oxalate-curcumin-based probe for micro- and macroimaging of reactive oxygen species in Alzheimer's disease, Proc Natl Acad Sci U S A 114 (47) (2017) 12384–12389.
[31] X. Zhang, Y. Tian, Z. Li, X. Tian, H. Sun, H. Liu, A. Moore, C. Ran, Design and synthesis of curcumin analogues for in vivo fluorescence imaging and inhibiting copper-induced cross-linking of amyloid beta species in Alzheimer's disease, J. Am. Chem. Soc. 135 (44) (2013) 16397–16409.
[32] M. Cui, M. Ono, H. Watanabe, H. Kimura, B. Liu, H. Saji, Smart near-infrared fluorescence probes with donor-acceptor structure for in vivo detection of β-amyloid deposits, J. Am. Chem. Soc. 136 (9) (2014) 3388–3394.
[33] C. Ran, X. Xu, S.B. Raymond, B.J. Ferrara, K. Neal, B.J. Bacskai, Z. Medarova, A. Moore, Design, synthesis, and testing of difluoroboron-derivatized curcumins as near-infrared probes for in vivo detection of amyloid-beta deposits, J. Am. Chem. Soc. 131 (42) (2009) 15257–15261.
[34] X. Zhang, Y. Tian, C. Zhang, X. Tian, A.W. Ross, R.D. Moir, H. Sun, R.E. Tanzi, A. Moore, C. Ran, Near-infrared fluorescence molecular imaging of amyloid beta species and monitoring therapy in animal models of Alzheimer's disease, Proc Natl Acad Sci U S A 112 (31) (2015) 9734–9739.
[35] A. Aslund, C.J. Sigurdson, T. Klingstedt, S. Grathwohl, T. Bolmont, D.L. Dickstein, E. Glimsdal, S. Prokop, M. Lindgren, P. Konradsson, D.M. Holtzman, P.R. Hof, F. L. Heppner, S. Gandy, M. Jucker, A. Aguzzi, P. Hammarström, K.P. Nilsson, Novel pentameric thiophene derivatives for in vitro and in vivo optical imaging of a plethora of protein aggregates in cerebral amyloidoses, ACS Chem. Biol. 4 (8) (2009) 673–684.
[36] R. Ni, Z. Chen, G. Shi, A. Villois, Q. Zhou, P. Arosio, R.M. Nitsch, P.R. Nilsson, J. Klohs, D. Razansky, Transcranial in vivo detection of amyloid-beta at single plaque resolution with large-field multifocal illumination fluorescence microscopy, bioRxiv (2020), 2020.02.01.929844.
[37] Y. Li, D. Xu, S.L. Ho, H.W. Li, R. Yang, M.S. Wong, A theranostic agent for in vivo near-infrared imaging of β-amyloid species and inhibition of β-amyloid aggregation, Biomaterials 94 (2016) 84–92.
[38] D. Hyde, R. de Kleine, S.A. MacLaurin, E. Miller, D.H. Brooks, T. Krucker, V. Ntziachristos, Hybrid FMT-CT imaging of amyloid-beta plaques in a murine Alzheimer's disease model, NeuroImage 44 (4) (2009) 1304–1311.
[39] X.L. Deán-Ben, G. Sela, A. Lauri, M. Kneipp, V. Ntziachristos, G.G. Westmeyer, S. Shoham, D. Razansky, Functional optoacoustic neuro-tomography for scalable whole-brain monitoring of calcium indicators, Light Sci. Appl. 5 (12) (2016), e16201.
[40] L.V. Wang, J. Yao, A practical guide to photoacoustic tomography in the life sciences, Nat. Methods 13 (8) (2016) 627–638.
[41] D. Razansky, A. Buehler, V. Ntziachristos, Volumetric real-time multispectral optoacoustic tomography of biomarkers, Nat. Protoc. 6 (8) (2011) 1121–1129.
[42] I. Olefir, A. Ghazaryan, H. Yang, J. Malekzadeh-Najafabadi, S. Glasl, P. Symvoulidis, V.B. O'Leary, G. Sergiadis, V. Ntziachristos, S.V. Ovsepian, Spatial and spectral mapping and decomposition of neural dynamics and organization of the mouse brain with multispectral optoacoustic tomography, Cell Rep. 26 (10) (2019) 2833–2846.e3.
[43] R. Ni, M. Rudin, J. Klohs, Cortical hypoperfusion and reduced cerebral metabolic rate of oxygen in the arcAbeta mouse model of Alzheimer's disease, Photoacoustics 10 (2018) 38–47.
[44] R. Ni, M. Vaas, W. Ren, J. Klohs, Non-invasive detection of acute cerebral hypoxia and subsequent matrix-metalloproteinase activity in a mouse model of cerebral ischemia using multispectral-optoacoustic-tomography, Neurophotonics 5 (1) (2018), 015005.
[45] Y. Liu, Y. Yang, M. Sun, M. Cui, Y. Fu, Y. Lin, Z. Li, L. Nie, Highly specific noninvasive photoacoustic and positron emission tomography of brain plaque with functionalized croconium dye labeled by a radiotracer †, Electronic supplementary information (ESI) available. See Click here for additional data file, Chem. Sci. 8 (4) (2017) 2710–2716, https://doi.org/10.1039/c6sc04798j.
[46] M. Knobloch, U. Konietzko, D.C. Krebs, R.M. Nitsch, Intracellular Abeta and cognitive deficits precede beta-amyloid deposition in transgenic arcAbeta mice, Neurobiol. Aging 28 (9) (2007) 1297–1306.
[47] Z. Chen, X.L. Dean-Ben, S. Gottschalk, D. Razansky, Performance of optoacoustic and fluorescence imaging in detecting deep-seated fluorescent agents, Biomed. Opt. Express 9 (5) (2018) 2229–2239.
[48] Z. Chen, X.L. Dean-Ben, S. Gottschalk, D. Razansky, Hybrid system for in vivo epifluorescence and 4D optoacoustic imaging, Opt. Lett. 42 (22) (2017) 4577–4580.
[49] J. Klohs, I.W. Politano, A. Deistung, J. Grandjean, A. Drewek, M. Dominietto, R. Keist, F. Schweser, J.R. Reichenbach, R.M. Nitsch, I. Knuesel, M. Rudin, Longitudinal assessment of amyloid pathology in transgenic ArcAbeta mice using multi-parametric magnetic resonance imaging, PLoS One 8 (6) (2013), e66097.
[50] J. Klohs, A. Deistung, G.D. Ielacqua, A. Seuwen, D. Kindler, F. Schweser, M. Vaas, A. Kipar, J.R. Reichenbach, M. Rudin, Quantitative assessment of microvasculopathy in arcAbeta mice with USPIO-enhanced gradient echo MRI, J. Cereb. Blood Flow Metab. 36 (9) (2016) 1614–1624.
[51] R. Ni, D.R. Kindler, R. Waag, M. Rouault, P. Ravikumar, R. Nitsch, M. Rudin, G. G. Camici, L. Liberale, L. Kulic, J. Klohs, fMRI reveals mitigation of cerebrovascular dysfunction by bradykinin receptors 1 and 2 inhibitor noscapine in a mouse model of cerebral amyloidosis, Front. Aging Neurosci. 11 (2019), 27-27.
[52] J. Klohs, A. Deistung, G. Ielacqua, A. Seuwen, D. Kindler, F. Schweser, M. Vaas, A. Kipar, J. Reichenbach, M. Rudin, Quantitative assessment of microvasculopathy in arcAβ mice with USPIO-enhanced gradient echo MRI, J. Cereb. Blood Flow Metab. 36 (9) (2016) 1614–1624.
[53] J. Klohs, C. Baltes, F. Princz-Kranz, D. Ratering, R.M. Nitsch, I. Knuesel, M. Rudin, Contrast-enhanced magnetic resonance microangiography reveals remodeling of

the cerebral microvasculature in transgenic ArcAbeta mice, J. Neurosci. 32 (5) (2012) 1705–1713.
[54] P. Arosio, R. Cukalevski, B. Frohm, T.P. Knowles, S. Linse, Quantification of the concentration of Aβ42 propagons during the lag phase by an amyloid chain reaction assay, J. Am. Chem. Soc. 136 (1) (2014) 219–225.
[55] S.I.A. Cohen, P. Arosio, J. Presto, F.R. Kurudenkandy, H. Biverstål, L. Dolfe, C. Dunning, X. Yang, B. Frohm, M. Vendruscolo, J. Johansson, C.M. Dobson, A. Fisahn, T.P.J. Knowles, S. Linse, A molecular chaperone breaks the catalytic cycle that generates toxic Aβ oligomers, Nat. Struct. Biol. 22 (2015) 207.
[56] M. Vaas, R. Ni, M. Rudin, A. Kipar, J. Klohs, Extracerebral tissue damage in the intraluminal filament mouse model of middle cerebral artery occlusion, Front. Neurol. 8 (2017) 85.
[57] Z. Chen, X.L. Deán-Ben, S. Gottschalk, D. Razansky, Hybrid system for in vivo real-time planar fluorescence and volumetric optoacoustic imaging, SPIE (2018).
[58] R. Ni, X.L. Dean-Ben, D. Kirschenbaum, M. Rudin, Z. Chen, A. Crimi, F. Voigt, P. R. Nilsson, F. Helmchen, R.M. Nitsch, A. Aguzzi, D. Razansky, J. Klohs, Whole brain optoacoustic tomography reveals strain-specific regional beta-amyloid densities in Alzheimer`s disease amyloidosis models, bioRxiv (2020), https://doi.org/10.1101/2020.02.25.964064.
[59] X.L. Dean-Ben, A. Ozbek, D. Razansky, Volumetric real-time tracking of peripheral human vasculature with GPU-accelerated three-dimensional optoacoustic tomography, IEEE Trans. Med. Imaging 32 (11) (2013) 2050–2055.
[60] L. Ding, X.L. Dean-Ben, D. Razansky, Efficient 3-D model-based reconstruction scheme for arbitrary optoacoustic acquisition geometries, IEEE Trans. Med. Imaging 36 (9) (2017) 1858–1867.
[61] A. Ozbek, X.L. Deán-Ben, D. Razansky, Realtime parallel back-projection algorithm for three-dimensional optoacoustic imaging devices, SPIE (2013).
[62] W. Ren, H. Skulason, F. Schlegel, M. Rudin, J. Klohs, R. Ni, Automated registration of magnetic resonance imaging and optoacoustic tomography data for experimental studies, Neurophotonics 6 (2) (2019) 1–10, 10.
[63] C. Xue, T.Y. Lin, D. Chang, Z. Guo, Thioflavin T as an amyloid dye: fibril quantification, optimal concentration and effect on aggregation, R. Soc. Open Sci. 4 (1) (2017), 160696.
[64] S. Prahl, https://omlc.org/spectra/hemoglobin/.
[65] R. Kayed, E. Head, F. Sarsoza, T. Saing, C.W. Cotman, M. Necula, L. Margol, J. Wu, L. Breydo, J.L. Thompson, S. Rasool, T. Gurlo, P. Butler, C.G. Glabe, Fibril specific, conformation dependent antibodies recognize a generic epitope common to amyloid fibrils and fibrillar oligomers that is absent in prefibrillar oligomers, Mol. Neurodegener. 2 (2007) 18.
[66] D.R. Thal, E. Ghebremedhin, C. Haass, C. Schultz, UV light-induced autofluorescence of full-length Abeta-protein deposits in the human brain, Clin. Neuropathol. 21 (1) (2002) 35–40.
[67] W.E. Klunk, B.J. Lopresti, M.D. Ikonomovic, I.M. Lefterov, R.P. Koldamova, E. E. Abrahamson, M.L. Debnath, D.P. Holt, G.-f. Huang, L. Shao, S.T. DeKosky, J. C. Price, C.A. Mathis, Binding of the positron emission tomography tracer Pittsburgh compound-B reflects the amount of amyloid-beta in Alzheimer's disease brain but not in transgenic mouse brain, J. Neurosci. 25 (46) (2005) 10598–10606.
[68] M. Ikonomovic, W. Klunk, E. Abrahamson, C. Mathis, J. Price, N. Tsopelas, B. Lopresti, S. Ziolko, W. Bi, W. Paljug, M. Debnath, C. Hope, B. Isanski, R. Hamilton, S. DeKosky, Post-mortem correlates of in vivo PiB-PET amyloid imaging in a typical case of Alzheimer's disease, Brain 131 (2008) 1630–1645.
[69] A. Manook, B.H. Yousefi, A. Willuweit, S. Platzer, S. Reder, A. Voss, M. Huisman, M. Settles, F. Neff, J. Velden, M. Schoor, H. von der Kammer, H.J. Wester, M. Schwaiger, G. Henriksen, A. Drzezga, Small-animal PET imaging of amyloid-beta plaques with [11C]PiB and its multi-modal validation in an APP/PS1 mouse model of Alzheimer's disease, PLoS One 7 (3) (2012), e31310.
[70] L. Helmfors, A. Boman, L. Civitelli, S. Nath, L. Sandin, C. Janefjord, H. McCann, H. Zetterberg, K. Blennow, G. Halliday, A.C. Brorsson, K. Kågedal, Protective properties of lysozyme on β-amyloid pathology: implications for Alzheimer disease, Neurobiol. Dis. 83 (2015) 122–133.
[71] R. Ni, P.G. Gillberg, A. Bergfors, A. Marutle, A. Nordberg, Amyloid tracers detect multiple binding sites in Alzheimer's disease brain tissue, Brain 136 (2013) 2217–2227.
[72] R. Ni, P.G. Gillberg, N. Bogdanovic, M. Viitanen, L. Myllykangas, I. Nennesmo, B. Langstrom, A. Nordberg, Amyloid tracers binding sites in autosomal dominant and sporadic Alzheimer's disease, Alzheimers Dement. 13 (4) (2017) 419–430.
[73] B. Bohrmann, L. Tjernberg, P. Kuner, S. Poli, B. Levet-Trafit, J. Näslund, G. Richards, W. Huber, H. Döbeli, C. Nordstedt, Endogenous proteins controlling amyloid beta-peptide polymerization. Possible implications for beta-amyloid formation in the central nervous system and in peripheral tissues, J. Biol. Chem. 274 (23) (1999) 15990–15995.
[74] R. Ni, J. Röjdner, L. Voytenko, T. Dyrks, A. Thiele, A. Marutle, A. Nordberg, In vitro characterization of the regional binding distribution of amyloid PET tracer Florbetaben and the glia tracers Deprenyl and PK1195 in autopsy Alzheimer brain tissue, J. Alzheimer Dis. (2021).
[75] J.P.F. Werner, Y. Huang, K. Mishra, R. Janowski, P. Vetschera, A. Chmyrov, D. Niessing, V. Ntziachristos, A.C. Stiel, Challenging a preconception: optoacoustic spectrum differs from the absorption spectrum of proteins and dyes for molecular imaging, bioRxiv (2020), 2020.02.01.930230.
[76] J. Klohs, J. Steinbrink, T. Nierhaus, R. Bourayou, U. Lindauer, P. Bahmani, U. Dirnagl, A. Wunder, Noninvasive near-infrared imaging of fluorochromes within the brain of live mice: an in vivo phantom study, Mol. Imaging 5 (3) (2006) 180–187.
[77] A. Taruttis, V. Ntziachristos, Advances in real-time multispectral optoacoustic imaging and its applications, Nat Photon 9 (4) (2015) 219–227.
[78] X.L. Dean-Ben, J. Robin, R. Ni, D. Razansky, Noninvasive Three-dimensional Optoacoustic Localization Microangiography of Deep Tissues, 2020.
[79] Y. Tang, J. Yao, 3D Monte Carlo Simulation of Light Distribution in Mouse Brain in Quantitative Photoacoustic Computed Tomography, arXiv:2007.07970, 2020.

Ruiqing Ni Ruiqing Ni obtained her BSc in Pharmacy at Fudan University, China. She completed a Ph.D. in Medicine at Karolinska Institutet, Sweden. She is currently junior group leader at ETH Zurich/University of Zurich. Her research focuses on the development of positron emission tomography, optical imaging and magnetic resonance imaging bio-markers for diagnosis of Alzheimer's disease.

Alessia Villois Alessia Villois obtained a BSc with honours in Chemical and Food Engineering from Polytechnic University of Turin (Italy) in July 2015. Afterwards, she did her MSc in Chemical and Bioengineering at ETH Zurich, where she was awarded the ETH Excellence Scholarship by the ETH Foundation. She began her PhD studies in September 2017 at the Institute of Chemical and Bioengineering under the supervision of Prof. Paolo Arosio and Prof. Andrew deMello.

Xose Luis Dean-Ben Xosé Luís Deán-Ben received the diploma in automatics and electronics engineering from the Universidade de Vigo in 2004. He received the PhD degree from the same university in 2009. Since 2010, he serves as a research fellow at the Lab for Multi-Scale Functional and Molecular Imaging at the Institute for Biological and Medical Imaging (IBMI), Helmholtz Center Munich. He is currently group leader and senior scientist at ETH Zurich. His major research interests are the development of new optoacoustic systems for preclinical and clinical applications and the elaboration of mathematical algorithms for fast and accurate imaging performance.

Zhenyue Chen Dr. Zhenyue Chen is a Marie Curie research fellow in the Institute of Pharmacology and Toxicology at University of Zurich. He received his Bachelor's degree in Electronic Science and Technology in 2010 and Ph. D. degree in Optical Engineering in 2016, both from Beijing Institute of Technology. During 2013–2015, he studied as a visiting Ph.D. student in College of Optical Sciences at the University of Arizona, working on fluorescence imaging and polarimetry. During 2016–2019, he worked as a postdoc in Technical University of Munich and Helmholtz Center Munich in Prof. Daniel Razansky's group, focusing on optoacoustic imaging techniques. His current work focuses on biomedical imaging with hybrid modalities including optics, optoacoustics and MRI.

Markus Vaas Markus Vaas studied biology and received a PhD in biomedical engineering from the ETH Zürich, Switzerland. He is Clinical Trial Monitor AT Clinical Trail Center University Zurich Hospital. In his research he applies optical imaging techniques to study the cellular inflammatory response (in particular the role of neutrophils) after ischemic stroke.

Stavros Stavrakis Stavros received his B.Sc. in Chemistry from the University of Crete (Greece) in 1999. In 2005 he gained his Ph.D. in Biophysical Chemistry from the University of Crete working on time-resolved vibrational spectroscopy of cytochrome oxidases. Prior to moving to Zurich in 2011 he was in the group of Prof. Stephen Quake at Stanford University as a Marie Curie fellow where he performed research on the development of new optical tools to improve the throughput of current single molecule DNA sequencing platforms. As a Marie Curie postdoctoral fellow he also worked in Dr David McGloin's lab at the University of Dundee, dealing with optical trapping of single cells in microfluidic chips. His current research interests are focused on applications of single molecule fluorescence detection, and optofluidics in biology. Currently he has a team of postdocs and students developing new microfluidic/ optofluidic platforms for single molecule enzymology, high-throughput imaging flow cytometry, ultrafast enzyme kinetics, fluorescence lifetime combined with droplet microfluidics and high-throughput microfluidic single-cell screening platforms.

Gloria Shi Gloria Shi obtained BSc and MSc in Biology and Neuroscience from ETH Zurich in Switzerland. She is currently PhD student at the University of Dundee. The work focuses on elucidating molecular mechanisms of LRRK2 in human stem cells.

Andrew deMello Andrew is currently Professor of Biochemical Engineering in the Department of Chemistry and Applied Biosciences at ETH Zurich and Head of the Institute for Chemical and Bioengineering. Prior to his arrival in Zurich he was Professor of Chemical Nanosciences and Head of the Nanostructured Materials and Devices Section in the Chemistry Department at Imperial College London. He obtained a 1st Class Degree in Chemistry and PhD in Molecular Photophysics from Imperial College London in 1995 and subsequently held a Postdoctoral Fellowship in the Department of Chemistry at the University of California, Berkeley working with professor Richard Mathies. His research interests cover a broad range of activities in the general area of microfluidics and nanoscale science. Primary specializations include the development of microfluidic devices for high-throughput biological and chemical analysis, ultra-sensitive optical detection techniques, nanofluidic reaction systems for chemical synthesis, novel methods for nanoparticle synthesis, the exploitation of semiconducting materials in diagnostic applications, the development of intelligent microfluidics and the processing of living organisms.

Chongzhao Ran Chongzhao Ran, PhD, is an Assistant Professor in Radiology at Massachusetts General Hospital and Harvard Medical School. He received a Master's degree in medicinal chemistry from China Pharmaceutical University and a PhD in medicinal chemistry from Shanghai Institute of Pharmaceutical Industry, China. He did his postdoctoral training at the University of Chicago and Harvard Medical School. Dr. Ran's research focuses on the development of molecular imaging probe and imaging technologies. Recently, his research group has successfully designed and synthesized secnd-generation PET tracers for amyloid beta species.

Daniel Razansky Daniel Razansky is Full Professor of Biomedical Imaging at the Faculty of Medicine, University of Zurich and Department of Information Technologies and Electrical Engineering, ETH Zurich. He earned PhD in Biomedical Engineering and MSc in Electrical Engineering from the Technion – Israel Institute of Technology and completed postdoctoral training in bio-optics at the Harvard Medical School. From 2007 until 2018 he was the Director of Multi-Scale Functional and Molecular Imaging Lab and Professor of Molecular Imaging Engineering at the Helmholtz Center and Technical University of Munich. Razansky's Lab pioneered a number of imaging technologies successfully commercialized worldwide, among them the multi-spectral optoacoustic tomography and hybrid optoacoustic ultrasound imaging. He has authored over 200 peer-review journal articles and holds 15 patented inventions in bio-imaging and sensing. He is a co-founding Editor of the Photoacoustics journal and serves on Editorial Boards of a number of journals published by Nature Publishing Group, Elsevier, IEEE and AAPM. He is also an elected Fellow of the OSA and SPIE.

Paolo Arosio Paolo Arosio received his master degree in Chemical Engineering from the Politecnico di Milano in 2007, and his doctoral degree from ETH Zurich in 2011. After his doctoral studies he moved to the group of Prof. Tuomas Knowles at the Department of Chemistry at the University of Cambridge, UK, where he was the recipient of a Swiss National Science Foundation fellowship for postdoctoral researchers and of a Marie Curie Intra-European fellowship for career development (IEF). In May 2016 he joined the Institute for Chemical and Bioengineering at ETH Zurich, where he is currently an Assistant Professor in Biochemical Engineering.

Jan Klohs Prof. Jan Klohs obtained a BSc degree in Chemistry at the University of Wales, Swansea, United Kingdom. He completed a MSc and Ph.D. in Medical Neurosciences at the Charité University Medicine Berlin, Germany. He is currently an assistant professor for preclinical imaging at the University of Zurich. His research focuses on the development of optical imaging and magnetic resonance imaging techniques, and investigations of preclinical models of brain disease.